Volume 971 15 October 2024 ISSN 1572-6657

ELSEVIER

Journal of Electroanalytical Chemistry

An International Journal
also devoted to
All Physicochemical Aspects of
Fundamental and Applied Electrochemistry

Editor-in-Chief:
X.H. Xia

Editors:
M. Opallo
R. Torresi
T. D. Chung
G. Xu

Available online at www.sciencedirect.com

ScienceDirect

In collaboration with
the International Society
of Electrochemistry

Journal of Electroanalytical Chemistry
Supports open access

Volume 971

15 October 2024

Download full issue

Previous vol/issue Next vol/issue

Receive an update when the latest issues in this journal are published

Sign in to set up alerts

Full text access
Editorial Board
Article 118637
View PDF

Research article Full text access
Investigation of electrochemical performance of Co-NC@CNT@MoS_2/S composite materials as cathodes for lithium-sulfur batteries
Zhifeng Zhao, Wangjun Feng, Wenting Hu, Yueping Niu, ... Li Zhang
Article 118559
View PDF Article preview

Research article Full text access
Effects on the structure and electrochemical reactivity of surface modified magnesium cobalt oxide
Kahla Missaoui, Karima Ferchichi, Noureddine Amdouni, Daniel Cosano, ... Gregorio F. Ortiz
Article 118561
View PDF Article preview

Review article Full text access
Oxygen vacancy defects enable high performance V_2O_5 cathode for aqueous zinc batteries: A mini review
Bibo Han, Xinhua Zheng, Mohsin Ali, Haocheng Wu, ... Shikai Liu
Article 118571
View PDF Article preview

Research article Full text access

Journal of Electroanalytical Chemistry

Submit your article Guide f

P. Arun Kumar, Aarathi Pradeep, Bipin Kumar G. Nair, T.G. Satheesh Babu, Punathil Vasu Suneesh
Article 118569

View PDF Article preview

Research article Full text access

Sustainable graphitic carbon derived from oil palm frond biomass for supercapacitor application: Effect of redox additive and artificial neural network-based modeling approach

Mohammad Ullah, Md. Munirul Hasan, Rasidi Roslan, Rajan Jose, Izan Izwan Misnon
Article 118570

View PDF Article preview

Research article Full text access

Novel electrochemical sensing platform based on zinc metal organic frameworks/carbon nanofiber nanocomposite for detection of creatinine in human urine

Km Shivangee Kushwaha, Abhinav Anand, Baban Dey, Md. Wasi Ahmad, ... Arup Choudhury
Article 118574

View PDF Article preview

Research article *Open access*

Electrochemical impedance analysis of the charge transfer mechanism on $Li_4Ti_5O_{12}$ surface in the presence or absence of the solid/electrolyte interface film

Saki Fukuma, Kazuki Yoshii, Mitsuharu Tabuchi, Satoshi Uchida
Article 118586

View PDF Article preview

Research article Full text access

High-performance Li-ion battery cathode: Mn-doped $LiFePO_4$ via solution combustion synthesis method

Chetana U. Mulik, Rohan S. Kamat, Xijue Wang, Chinmayee Padwal, ... Lata D. Jadhav
Article 118568

View PDF Article preview

Research article Full text access

Selecting optimal carbon inks for fabricating high-performance screen-printed electrodes for diverse electroanalytical applications

Hanan Barich, Olivier Voet, Nick Sleegers, Jonas Schram, ... Karolien De Wael
Article 118585

View PDF Article preview

Research article Full text access

Correlating crystallinity regulation in spinel oxides and catalytic activity in electrocatalytic water oxidation

Pengkun Wei, Wenhui Zhang, Mengyuan Luo, Miao Yu, ... Ruijuan Duan
Article 118565

View PDF Article preview

Research article Full text access

Preparation and electrochemistry study of a new Ti-based PbO_2 electrode with Ta-Ti-Sn(Ru)O_x interlayer in Cu electrowinning

Cheng Jiang, Xionghui Xie, Chao Gao, Buming Chen, ... Ruidong Xu
Article 118573

Journal of Electroanalytical Chemistry

Submit your article Guide f

View PDF Article preview

Research article Full text access

Targeted microorganism detection with molecularly imprinted polymer biosensors

Hüseyin Oğuzhan Kaya, Yamaç Tekintaş, Fatma Kurul, Arif E. Cetin, Seda Nur Topkaya

Article 118575

View PDF Article preview

Research article Full text access

In_2O_3 electrochemical transistors based on $PtAu_4$/RGO nanocomposites functionalized gate for highly sensitive nitrite detection

Ruling Wang, Zhiwei Cai, Hong Zhu, Lei Wang, ... Gang Chang

Article 118572

View PDF Article preview

Research article *Open access*

A versatile electrochemical cell for *in-situ* GI-XRD measurements on lab-scale XRD devices

Fabian Froech, Sabine Kubicek, Werner Artner, Michael Nelhiebel, ... Guenter Fafilek

Article 118591

View PDF Article preview

Research article Full text access

pH and potential-controlled multi-modal mass transport in block copolymer nanochannel membranes

Soongyu Han, Yerin Bang, Jeongse Yun, Seol Baek, ... Seung-Ryong Kwon

Article 118564

View PDF Article preview

Research article Full text access

Assessing the viability of chromium (II) as a corrosion inhibitor for 316H stainless steel in NaF-BeF_2 molten salt

Yong Zuo, Wen Peng, Hao Peng, Wei Huang, Yu Gong

Article 118567

View PDF Article preview

Research article Full text access

Synthesis and electrochemical properties of microcanals Mg-S-Cu-S as an electrode material for energy storage applications

M. Ahsan Ali, A. Farid, A. Rasheed, Misbah Yousaf, ... Frank Marken

Article 118588

View PDF Article preview

Research article Full text access

Carbon nanofibers embedded in nanopores decorated graphite felt electrodes for enhanced vanadium redox flow batteries performance

Liying Wang, Yu Zhao, Huang Liu, Tong Wang, ... Puiki Leung

Article 118524

View PDF Article preview

Research article Full text access

Journal of Electroanalytical Chemistry

Submit your article Guide f

High aspect ratio copper nanowires modified screen-printed carbon electrode for interference-free non-enzymatic detection of serum creatinine in neutral medium

Chandhana J.P., Roshith M., Suneesh Punathil Vasu, Darbha V. Ravi Kumar, Satheesh Babu T.G.

Article 118605

View PDF Article preview

Research article Full text access

Study of the application of a Cu_2O thin film as non-enzymatic amperometric glucose sensor

Francisco Figueredo, Rodrigo Henríquez, Eduardo Muñoz, Cristopher Heyser, ... Paula Grez

Article 118584

View PDF Article preview

Research article Full text access

Design and construction of V_6O_{13}/C nanorods as high-performance cathode material for aqueous zinc-ion batteries

Liying Zheng, Laiying Jing, Lufan Yang, Xinting Yu, ... Yunqiang Zhang

Article 118596

View PDF Article preview

Research article Full text access

Improving the electrocatalytic activity of the copper (II) metal-organic framework by functionalized imidazolate linker and functionalized carbon nanoparticles for detection of acyclovir

Biuck Habibi, Ali Pashazadeh, Sara Pashazadeh

Article 118595

View PDF Article preview

Research article Full text access

Preparing a binder-free cathode composed of NMC811/sulfonated reduced graphene oxide sheets/carbon black via in-situ electrophoretic deposition to enhance cyclability of Li-ion batteries

Fatemeh Poursalehi, Mehran Javanbakht, Ahmad Ahmadi Daryakenari, Biao Gao

Article 118593

View PDF Article preview

Review article Full text access

Advances in ion doping and intercalation strategies for the performance of manganese-based oxides in aqueous zinc-ion batteries

Kaixuan Ma, Guangfeng Liang, Caihong Feng, Yun Zhao

Article 118587

View PDF Article preview

Research article Full text access

Enhanced electron transfer kinetics via constructing co-catalytic system of cerium oxide and carbon dots enabling efficient electrosynthesis of hydrogen peroxide in neutral media

Weijie Yuan, Jiacheng Li, Huiyu Yang, Ziliang Chen, ... Zhenhui Kang

Article 118604

View PDF Article preview

Research article Full text access

Sulfur vacancy riched pure 2H phase VS_2 for efficient electrocatalytic hydrogen evolution

Journal of Electroanalytical Chemistry

Submit your article

Guide f

Article 118594

View PDF Article preview

Previous vol/issue

Next vol/issue

About this publication

ISSN: 1572-6657

Copyright © 2025 Elsevier B.V. All rights are reserved, including those for text and data mining, AI training, and similar technologies.

ELSEVIER

All content on this site: Copyright © 2025 Elsevier B.V., its licensors, and contributors. All rights are reserved, including those for text and data mining, AI training, and similar technologies. For all open access content, the relevant licensing terms apply.

RELX™

Journal of Electroanalytical Chemistry 971 (2024) 118604

Contents lists available at ScienceDirect

Journal of Electroanalytical Chemistry

journal homepage: www.elsevier.com/locate/jelechem

Enhanced electron transfer kinetics via constructing co-catalytic system of cerium oxide and carbon dots enabling efficient electrosynthesis of hydrogen peroxide in neutral media

Weijie Yuan [a], Jiacheng Li [a], Huiyu Yang [a], Ziliang Chen [a,*], Zhiwei Liu [a], Hui Huang [a,*], Yang Liu [a], Zhenhui Kang [a,b,*]

[a] Institute of Functional Nano & Soft Materials (FUNSOM), Jiangsu Key Laboratory for Carbon-Based Functional Materials & Devices, Soochow University, 199 Ren'ai Road, Suzhou 215123, China
[b] Macao Institute of Materials Science and Engineering (MIMSE), MUST-SUDA Joint Research Center for Advanced Functional Materials, Macau University of Science and Technology, Taipa 999078, Macau

ARTICLE INFO

Keywords:
Rare earth oxide
Coupling effect
Charge transfer kinetics
Catalytic performance
Two electron oxygen reduction

ABSTRACT

The sluggish kinetics coupled with the competition of four-electron pathway in neutral media diminishes the production efficiency of hydrogen peroxide (H_2O_2) via the two-electron oxygen reduction reaction ($2e^-$ ORR). To address this dilemma, this contribution proposes one electron modulation strategy to expedite the charge transfer capability by integrating carbon dots with CeO_2 (CDs/CeO_2) for the efficient neutral electrosynthesis of H_2O_2. It was found that the integration could effectively bolster both the activity and selectivity of $2e^-$ ORR on CDs and CeO_2. Remarkably, the highest $2e^-$ selectivity could reach up to 92 % for the optimized CDs/CeO_2, substantially surpassing that (77 %) of pristine CeO_2, together with about 1.5 times enhancement of activity. Meanwhile, it also delivered a superior long durability at 20 mA cm^{-2} for 24 h and a high Faraday efficiency of 97 %. Further *in-situ* transient potential scanning (TPS) technique revealed that the pseudo-capacitance and charge storage capacity of CeO_2 were significantly tuned by CDs during dynamic ORR process, being conducive to the reaction kinetics and the $2e^-$ selectivity. The findings in this work not only extends the co-catalytic system based on CDs and rare earth materials for $2e^-$ ORR, but also offers novel insights into correlation between their electron distribution dynamics and $2e^-$ ORR performance.

1. Introduction

As one of the most important chemicals in the world, hydrogen peroxide (H_2O_2) has been widely deployed as an eco-sustainable oxidant in several key areas including printing, medicine, environmental remediation and energy conversion [1–3]. Currently, the anthraquinone auto-oxidation process remains a prevalent method, but which is suffering from the high energy consumption, complex production process, inevitable by-products and large amounts of chemical waste [4–6]. Within this context, extensive researches are ongoing to develop more sustainable and cost-effective methods for H_2O_2 production. The electrochemical synthesis of H_2O_2 via the two-electron oxygen reduction reaction ($2e^-$ ORR) is green and convenient, offering reduced energy demands and environmental footprints [7–9]. Meanwhile, it is an available pathway to achieve customer-oriented on-site synthesis of H_2O_2, which has been identified as a promising alternative to the energy-consuming anthraquinone process [10–12]. The $2e^-$ ORR can be carried out in acidic, alkaline or neutral media [13]. Particularly, neutral environment is more attractive because of its environmentally friendly properties, by which corrosion can be greatly alleviated, and the potential cost of the electrolyzer can be reduced [14–16]. However, under neutral conditions, the ion diffusion in the electrolyte is much weaker, leading to the poor electron transfer ability and thus the sluggish kinetics [17–19]. In addition, the electrochemical synthesis of H_2O_2 is competed by the four-electron pathway during oxygen reduction reaction ($4e^-$ ORR), resulting in the lower efficiency for producing H_2O_2 [20,21]. Therefore, it is of great significance to search a highly selective, active and durable electrocatalyst for the electrochemical synthesis of

* Corresponding authors at: Institute of Functional Nano & Soft Materials (FUNSOM), Jiangsu Key Laboratory for Carbon-Based Functional Materials & Devices, Soochow University, 199 Ren'ai Road, Suzhou 215123, China (Z. Kang).
E-mail addresses: zlchen@suda.edu.cn (Z. Chen), hhuang0618@suda.edu.cn (H. Huang), zhkang@suda.edu.cn (Z. Kang).

https://doi.org/10.1016/j.jelechem.2024.118604
Received 5 May 2024; Received in revised form 5 August 2024; Accepted 22 August 2024
Available online 28 August 2024
1572-6657/© 2024 Elsevier B.V. All rights are reserved, including those for text and data mining, AI training, and similar technologies.

H_2O_2.

Over the past decade, rare earth metal oxides have received extensive attention as co-catalysts to improve the electrocatalytic performance of transition metal active components due to their excellent corrosion resistance, abundant oxygen vacancy, and high oxygen storage capacity [22,23]. Recently, as a pioneering work, Hota et al. found that several rare earth oxides have good intrinsic catalytic activity towards alkaline $2e^-$ ORR. Typically, Nd_2O_3 mixed with carbon ink showed 91.91 % selectivity for the H_2O_2 production [24]. Following this observation, Chang et al. recently reported a CeO_2 nanoarchitecture, The CeO_2 nanoarchitecture delivers 83 % H_2O_2 selectivity and the H_2O_2 yield reaches 632 mmol $g_{cat}^{-1}h^{-1}$ after 4 h continuous $2e^-$ ORR reaction at 0.5 V, and the faradaic efficiency could reach up to 95.3 % in 0.1 M KOH [25]. Obviously, these investigations are encouraging, offering the chance for exploring the rare earth metal oxides as advanced $2e^-$ ORR electrocatalysts. Nevertheless, the electrocatalysts presented in these studies are confined to alkaline environment, and there remains a lack of literature regarding rare earth oxide-based electrocatalysts for applications in neutral pH conditions. Moreover, how to improve the reaction kinetics of rare earth oxides for $2e^-$ ORR in neutral media is still a formidable challenge.

On the other hand, carbon dots (CDs) are a new type of material with the diameter of less than 10 nm, with rich functional groups (–COOH, –OH, –C═O, etc.), and has broad application prospects in luminescence, biology, catalysis and other fields [26]. As a co-catalyst, CDs can exert a significant impact on the electron transfer of coupling system [27,28]. In prior research, Song et al. demonstrated that the modification of MoP with nitrogen-doped CDs could effectively enhance the charge transfer ability, leading to the enhanced HER catalytic activity close to that of commercial Pt/C catalysts (32 mV), and corroborating the efficiency of employing CDs as one subunit to modulate electrocatalytic property of system [29]. Inspired by this finding, Wu et al. improved the $2e^-$ ORR catalytic activity of In_2O_3 by using CDs as a co-catalyst to regulate the electron transport kinetics of In_2O_3. The H_2O_2 selectivity of optimal In_2O_3/CDs-10 is close to 100 %, which is much higher than that of pure In_2O_3 (72 %) in 0.1 M KOH [30]. Motivated by these appealing observations, one can envision that if the rare earth oxides and CDs can be combined, a favorable electron transfer capability can be gained for the system, and thus enhanced electrocatalytic $2e^-$ ORR performance in neutral media. Furthermore, although the electron transfer kinetics has been considered to be one of the most important factors affecting the selectivity of oxygen reduction [31], to our knowledge, the charge distribution dynamics during $2e^-$ ORR for catalytic system, has never been pursued.

Bear the above-mentioned points in mind, in this work, we synthesized CDs/CeO_2 composites to study their $2e^-$ ORR performance in neutral media and investigate the corresponding electron distribution dynamics. As expected, the H_2O_2 selectivity for the optimal composite (10-CeO_2/CDs) can reach up to as high as 92 %, which is much higher than that of CeO_2 (77 %). Moreover, the limited current density achieved by the 10-CeO_2/CDs composite is approximately 1.5 times greater than that of pristine CeO_2, signifying a substantial enhancement in the activity of CeO_2 facilitated by CDs. Concurrently, the H_2O_2 generation efficiency for the 10-CeO_2/CDs system reaches 97 %, in conjunction with an impressive durability sustained over a 24-hour period. Additionally, we employed a home-made transient potential scanning (TPS) technique to analyze the differences in electron distribution dynamics between CeO_2 and the 10-CeO_2/CDs composite. Our findings elucidate that CDs can significantly modulate the electron distribution within CeO_2 by altering its pseudo-capacitance, charge transfer dynamics, and oxygen adsorption capabilities. This feasible tuning leads to a 10-CeO_2/CDs catalyst that displays increased selectivity and activity. Thus, our research highlights the strategic manipulation of charge transfer as an effective approach to enhance the catalytic performance. Moreover, it confirms that analyzing the dynamics of electron distribution in catalytic systems is a viable method for unraveling complex mechanisms in intricate environments, guiding the development of highly efficient electrocatalysts.

2. Experimental section

2.1. Materials

Cerium nitrate ($Ce(NO_3)_3{\cdot}6H_2O$, 98.0 %), ethanol (99.5 %) and sodium hydroxide (NaOH, > 95 %) were purchased from Sinopharm Chemical Reagent Co. Ltd (China). These materials were used in this study without further purification. Nafion perfluorinated resin solution (5 wt%) was purchased from Adamas-Betas; Anion exchange membrane was purchased from Fumasep. Milli-Q ultrapure water (Millipore, ≥ 18.25 MΩ cm^{-1}) was used throughout the work.

2.2. Synthesis of CDs, CeO_2 and CDs/CeO_2

CDs was prepared using graphite rod as carbon source by electrolysis method. DC regulated power supply with a fixed voltage of 30 V was used as the power supply, and pure water was used as the electrolyte for electrolysis. After 60 days of electrolysis, the black solution was collected and filtered to remove large carbon particles. Finally, the black solution was freeze-dried to obtain CDs.

For the synthesis of CeO_2, 0.88 g $Ce(NO_3)_3{\cdot}6H_2O$ was added to 15 mL 6 M NaOH solution by ultrasound until completely dissolved. Then the solution was transferred into a 50 mL Teflon-lined stainless steel autoclave, heated at 180 °C for 24 h, cooled to room temperature, and the product was collected, washed with H_2O/ethanol several times, and dried and ground to obtain CeO_2 powder. 0.1 g CeO_2 powder was added into 0 mg CDs, 5 mg CDs, 10 mg CDs and 15 mg CDs respectively, and dispersed in 5 mL pure water, stirring overnight until evenly mixed. Under N_2 protection, samples with different mixing ratios of CDs were calcined in a tube furnace at 300 °C for 2 h to obtain CeO_2, 5-CDs/CeO_2, 10-CDs/CeO_2, 15-CDs/CeO_2.

2.3. Electrochemical protocol

H_2O_2 selectivity and number of transferred electrons (n) were obtained via rotating ring-disk electrode (RRDE) measurement. All the electrochemical measurements were carried out on CHI760E electrochemical station (Chenghua, Shanghai). A standard three-electrode setup was used with the RRDE loaded with catalyst as the working electrode, carbon rod as the counter electrode, and saturated calomel electrode (SCE) as the reference electrode. The ORR test was performed in an O_2 saturated electrolyte (0.1 mol/L K_2SO_4). Catalyst ink was prepared by ultrasonic mixing of a mixture of 3.6 mg catalyst, 1 mL of 0.5 wt.% Nafion solution and 0.4 mg carbon black. Then, 6.2 μL of catalyst ink was poured onto the RRDE electrode and dried at room temperature to obtain a catalyst loading of 0.2 mg cm^{-2}. Linear scanning voltammetry (LSV) was used to investigate the ORR activity and selectivity of different catalysts at 0.1 M K_2SO_4 and 1600 rpm.H_2O_2 selectivity and electron transfer number were calculated as follows:

$$n = 4\frac{I_D}{I_D + I_R/N}$$

$$H_2O_2(\%) = 200\frac{I_R/N}{I_D + I_R/N}$$

where I_R represents the ring current, I_D represents the absolute value of disk current and the collection efficiency (N) of the RRDE is determined as 0.37 [32].

Electrocatalytic H_2O_2 production on hydrophobic carbon paper loaded with catalysts (0.05 mg cm^{-2}) was performed in a H-Cell filled with 40 mL electrolyte (0.1 M K_2SO_4). In this setup, the working electrode is the carbon paper of the supported catalyst, with platinum foil as

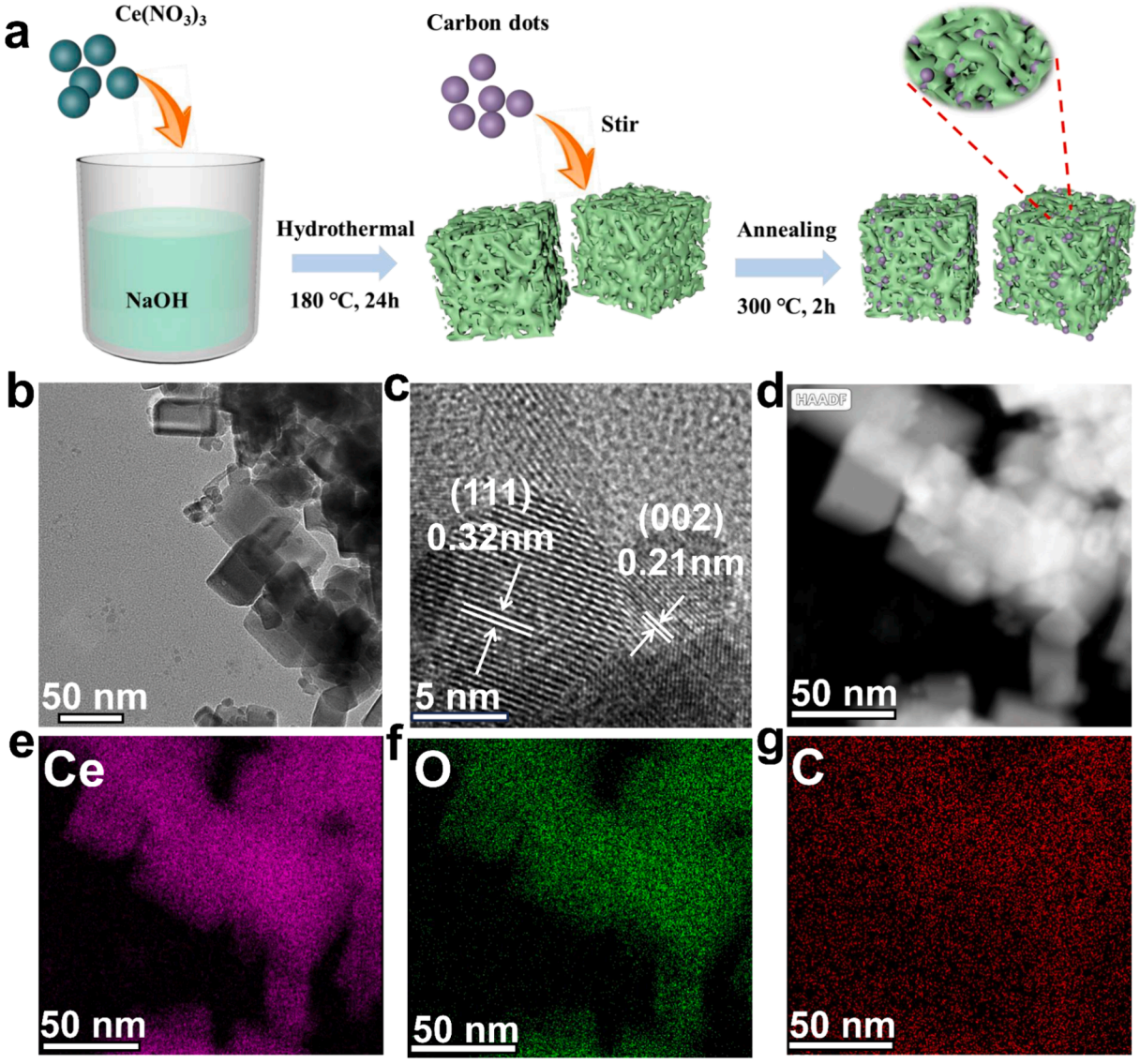


Fig. 1. (a) The schematic diagram for the synthesis of CDs/CeO_2. (b) TEM image of 10-CDs/CeO_2 at low magnification. (c) TEM image of 10-CDs/CeO_2 at high magnification. (d) HAADF-STEM image, and (e-g) Element mapping images of 10-CDs/CeO_2.

the reverse electrode. The catalyst ink was prepared by mixing 0.5 mg catalyst with 0.1 mL 5 % nafion, 0.6 mL H_2O and 0.3 mL ethanol. The reaction was evaluated by chronopotentiometry with a reversible hydrogen electrode (RHE) at a constant potential of 0 V for testing the 1800 s without ohmic drop correction. The yield of H_2O_2 was determined by potassium permanganate ($KMnO_4$) titration.

1 mL electrolyte was extracted, and the generated H_2O_2 concentration was quantified by titration with $KMnO_4$ solution (0.02 mol/L). H_2O_2 productivity was determined by its reaction with MnO_4^-:

$$2MnO_4^- + 5H_2O_2 + 6H^+ \rightarrow 2Mn^{2+} + 5O_2 + 8H_2O$$

The faraday efficiency (FE) and yield (YR) of H_2O_2 generation of the H-Cell were calculated as follows: $FE = \frac{2*96500*M_{H_2O_2}}{C}$, $YR = \frac{M_{H_2O_2}}{g_{cat}*t}$, where M_{H2O2} is the number of moles of H_2O_2 generation, C is the total charge consumed, t is the electrolytic time, and g_{cat} is the catalyst mass.

In order to verify the accuracy of the determination of hydrogen peroxide concentration, eFOX solution standard colorimetry was used to determine the concentration of H_2O_2 during the catalysis process and the results were compared with potassium permanganate titration. The preparation method for eFOX solution: $Fe(NH_4)_2(SO_4)_2{\cdot}6H_2O$ (98.05 mg), D-sorbitol (18.20 mg), and xylenol orange (71.65 mg) were dissolved in a mixture of ultrapure H_2O (1000 mL), ethanol (10 mL), and H_2SO_4 (98 %, 1.36 mL). Subsequently, 1 mL the cathode solution obtained after reaction at 0 V *vs.* RHE voltage for 1800 s in H-Cell was mixed with 10 mL the prepared eFOX solution and then stood for 1 h. The characteristic absorption spectrum of the mixture at 554 nm was monitored by UV–Vis spectroscopy, and the concentration of H_2O_2 was quantitatively determined. The calibration curve was obtained in the previous work: $A = 0.000414603*C_1 + 0.00327$ [40], A of absorbance for solution, C_1 for H_2O_2 concentration in the solution. H_2O_2 concentration in the reaction liquid of $C_2 = \frac{0.011*C_1}{0.001}$, H_2O_2 yield of catalysts for $YR = \frac{C_2*V}{m*t}$.

2.4. Transient potential scanning (TPS) test

To investigate the kinetics of charge distribution on the catalyst surface, a self-designed TPS device was employed. The working electrode (glass-carbon electrode) was connected to the positive electrode, while the reference electrode (saturated calomel electrode) and counter electrode (carbon rod) were connected to the negative electrode. The fixed capacitor could be charged at different voltages, and upon full

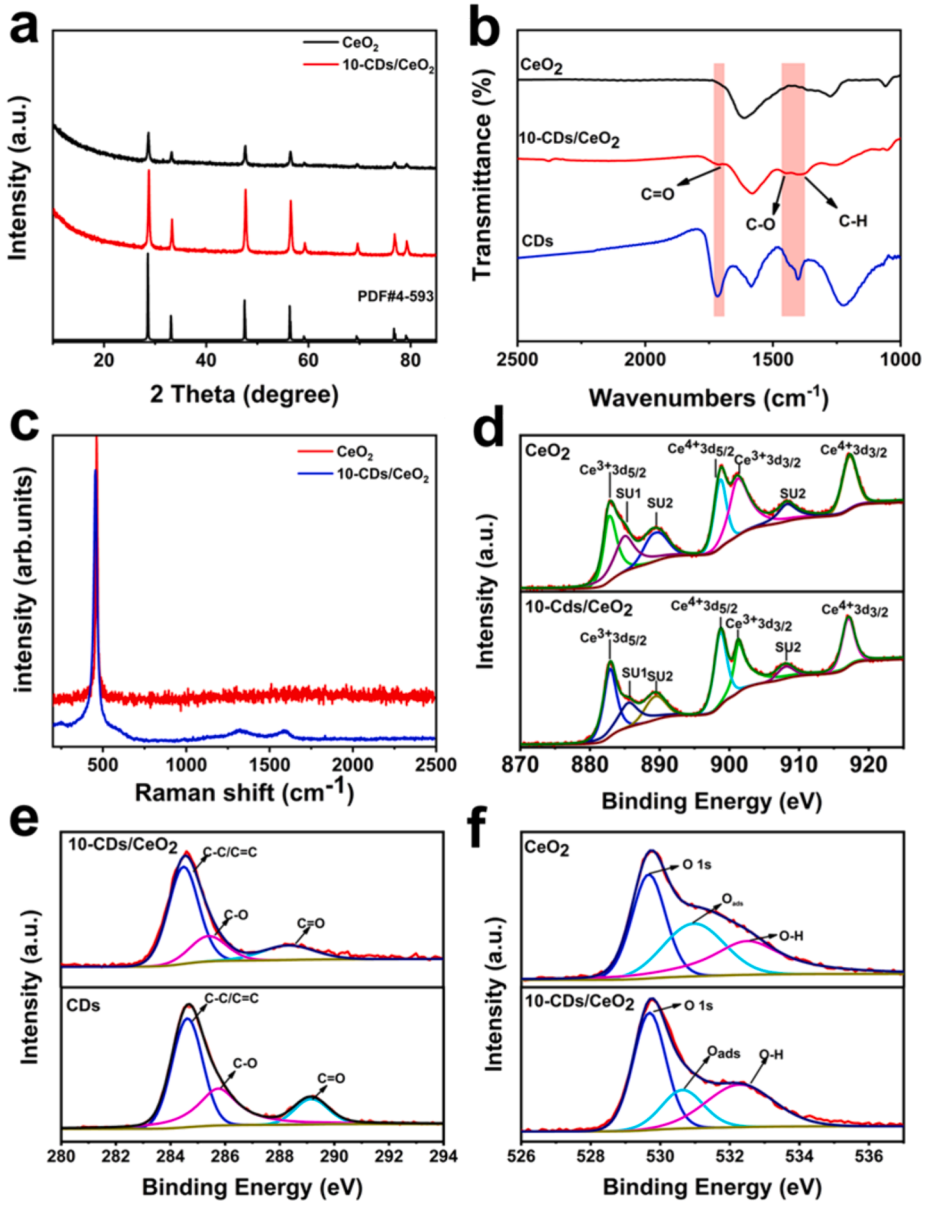


Fig. 2. (a) The XRD patterns of CeO_2 and 10-CDs/CeO_2. (b) FT−IR spectra of CeO_2, 10-CDs/CeO_2 and CDs. (c) Raman spectra of CeO_2, 10-CDs/CeO_2 and CDs. (d) Ce 3d XPS spectra of CeO_2 and 10-CDs/CeO_2. (e) C 1s XPS spectra of CDs and 10-CDs/CeO_2. (f) O 1s XPS spectra of CDs and 10-CDs/CeO_2.

charge, it is connected to the test circuit system, allowing the collection of current signals to analyze charge transfer at the catalyst interface by adjusting the voltage.

3. Results and discussion

3.1. Morphology and structural characterization

Fig. 1a schematically illustrated the preparation of CDs/CeO_2. Firstly, CeO_2 nanocubes were obtained by one-pot hydrothermal method using $Ce(NO_3)_3$ as Ce source in NaOH solution (Fig. S1). Then, CeO_2 and CDs were mixed evenly by stirring followed by annealing to obtain CDs/CeO_2 composites. Transmission electron microscopy (TEM) image of the 10-CDs/CeO_2 composites is shown in Fig. 1b, from which these composites are in the shape of nanocubes. Being well consistent with the TEM result, FESEM images of 10-CDs/CeO_2 also show the cubic morphology. Note that CeO_2, 5-CDs/CeO_2, and 15-CDs/CeO_2 all show the similar morphologies to those of 10-CDs/CeO_2 (Fig. S2). High-resolution TEM (HRTEM) image of the 10-CDs/CeO_2 composite displays a lattice spacing of 0.21 nm in the marginal region (Fig. 1c), which can be assigned to the (002) plane of CDs. Moreover, a lattice spacing of 0.32 nm is also observed for the nanocube near to the CD, which can be assigned to the (1 1 1) plane of CeO_2. These results well demonstrate the coupling between CDs and CeO_2. HAADF-STEM image (Fig. 1d) and corresponding elemental mapping results (Fig. 1e-g) also confirm the presence of C, Ce, and O within the 10-CDs/CeO_2 composite.

On the other hand, the XRD patterns of CeO_2 and 10-CDs/CeO_2 are shown in Fig. 2a. Obviously, the peaks at 28.5°, 33.1°, 47.5°, 56.3°, 69.4°, 76.7°, 79.1° and 88.4° can be identified, which are well matched with those of the standard card JCPDS No. 04-0593 of CeO_2 phase. The XRD pattern of 10-CDs/CeO_2 shows the very similar peaks at the corresponding position. Note that no diffraction peaks belonging to carbon can be found, which may be due to the poor crystallization of CDs and the overlap of diffraction peaks belonging to the CeO_2 (111) plane at 28.5° and the carbon (002) plane at around 28°. Similarly, other CDs/CeO_2 composites show the similar XRD patterns (Fig. S3). Nevertheless, the signals for CDs can be extracted from Fourier Transform infrared (FT-IR), Raman spectra and X-ray photoelectron spectroscopy (XPS).

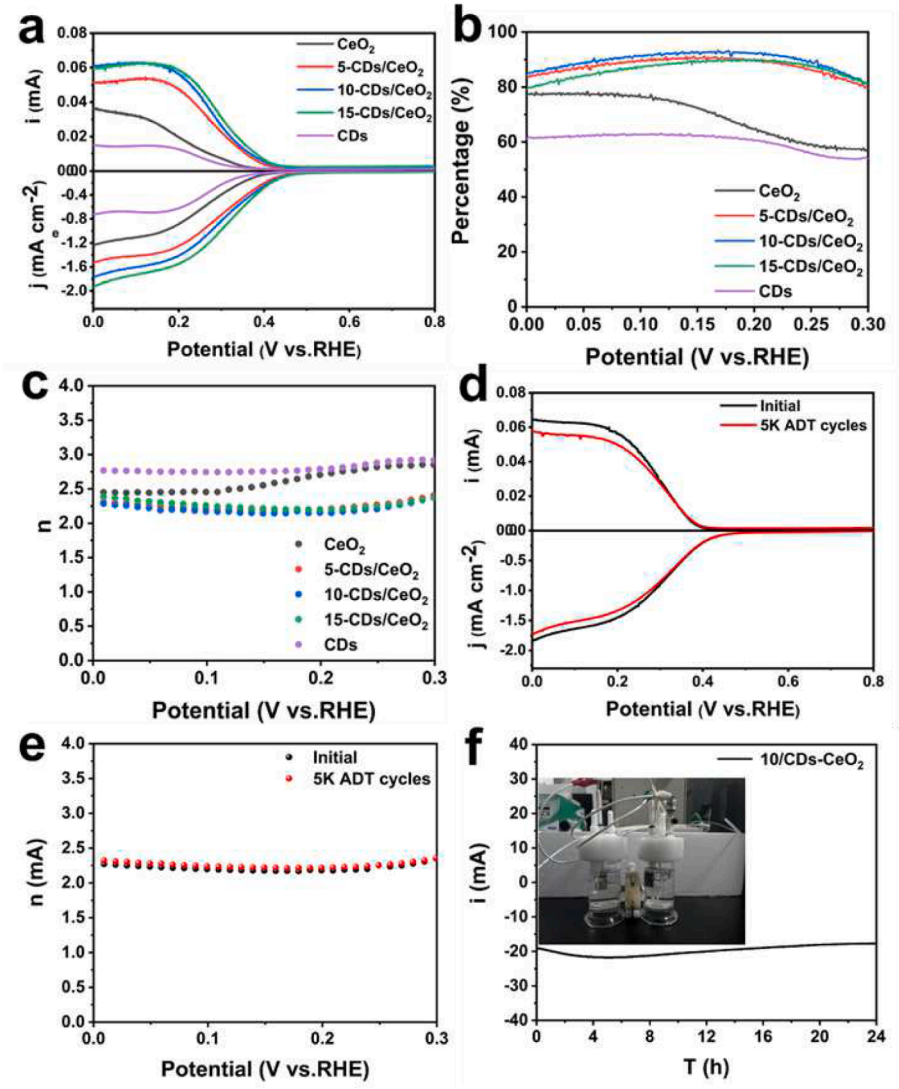


Fig. 3. (a) LSV curves of CeO_2, 5-CDs/CeO_2, 10-CDs/CeO_2, 15-CDs/CeO_2 and CDs. The bottom half part represents the disk current density, while the upper half part represents the ring current. (b) The calculated H_2O_2 selectivity of the five samples. (c) The calculated electron transfer number of the five samples. (d) Comparison of LSV curves of 10-CDs/CeO_2 after initial and 5 K ADT cycles. (e) The calculated electron transfer number of 10-CDs/CeO_2 after initial and 5 K ADT cycles. (f) The chronoamperometry curve of the 10-CDs/CeO_2 in 24 h. Inset in f shows the H-Cell apparatus for testing.

Specifically, Fig. 2b shows the FT-IR spectra of CeO_2, 10-CDs/CeO_2, and CDs. Compared with CeO_2, several significant new absorption peaks were observed at 1720, 1450, and 1388 cm^{-1} for 10-CDs/CeO_2, which can be identified as C═O, C—O, and C—H bonds for stretching vibrations, respectively [33]. Similar properties have been found for other CDs/CeO_2 composites (Fig. S4). These observations indicate that there are abundant oxygen-containing functional groups on CDs, which can be considered to be conducive to tuning catalyst surfaces and improving catalytic performance. Fig. 2c shows the Raman spectra of CeO_2 and 10-CDs/CeO_2. Compared with CeO_2, two peaks of 10-CDs/CeO_2 can be observed at 1320 and 1585 cm^{-1}, which belong to the D and G bands of CDs [34]. This proves again the synthesis 10-CDs/CeO_2 composites.

The detailed elemental information of the sample surface was checked by XPS. Fig. 2d shows the 3d nuclear level peak of Ce in CeO_2 and 10-CDs/CeO_2, where Ce 3d spectra of CeO_2 can be divided into 7 groups. Due to its highly non-stoichiometric properties, two valence states Ce^{3+} and Ce^{4+} exist in CeO_2. The main peak binding energies of Ce^{4+} $3d_{3/2}$ and Ce^{4+} $3d_{5/2}$ were 917.1 and 898.7 eV, respectively. Ce^{3+} $3d_{3/2}$ and Ce^{3+} $3d_{5/2}$ have binding energies of 901.3 and 882.8 eV, respectively. The other three satellite lines SU1 and SU2, which means "concussion", show 908.4 eV and 885.0 eV and 889.6 eV respectively on Ce^{3+} $3d_{3/2}$. These spectra are fully consistent with those previously reported, confirming the coexistence of Ce^{4+} and Ce^{3+} [35]. In addition, from the Ce three-dimensional nuclear level peak in 10-CDs/CeO_2, it can be observed that the ratio of the integral area of Ce^{3+} $3d_{3/2}$ and Ce^{3+} $3d_{5/2}$ main peaks to the integral area of Ce^{4+} $3d_{3/2}$ and Ce^{4+} $3d_{5/2}$ main peaks is 0.8412, which is smaller than that of CeO_2 1.5. This means that the presence of CeO_2 contributes to the transform of Ce^{3+} to Ce^{4+}. Fig. 2e shows the C 1s spectra of CDs and 10-CDs/CeO_2, in which three peaks of C—C/C═C, C—O and C═O can be observed at 284.6, 285.7 and 289.1 eV in the C 1s spectra of CDs, which are in well agreement with the FT-IR results [36]. The C 1s spectra of 10-CDs/CeO_2 shift to the lower energy level, which is related to the change of Ce valence state in CeO_2. As shown in Fig. 2f, the main XPS peak of O 1s is superimposed near 529.7 eV. The adsorbed oxygen in CeO_2 has a peak value of 531 eV [37]. The O 1s peak at 532.5 eV is independent of the presence of Ce^{3+} or Ce^{4+}. It has been suggested that the peak of 532.5 eV is caused by the OH on the surface [38]. Similarly, the XPS results of 5-CDs/CeO_2 and 15-CDs/CeO_2 were also obtained (Figs. S5, S6), which were consistent with those results for 10-CDs/CeO_2.

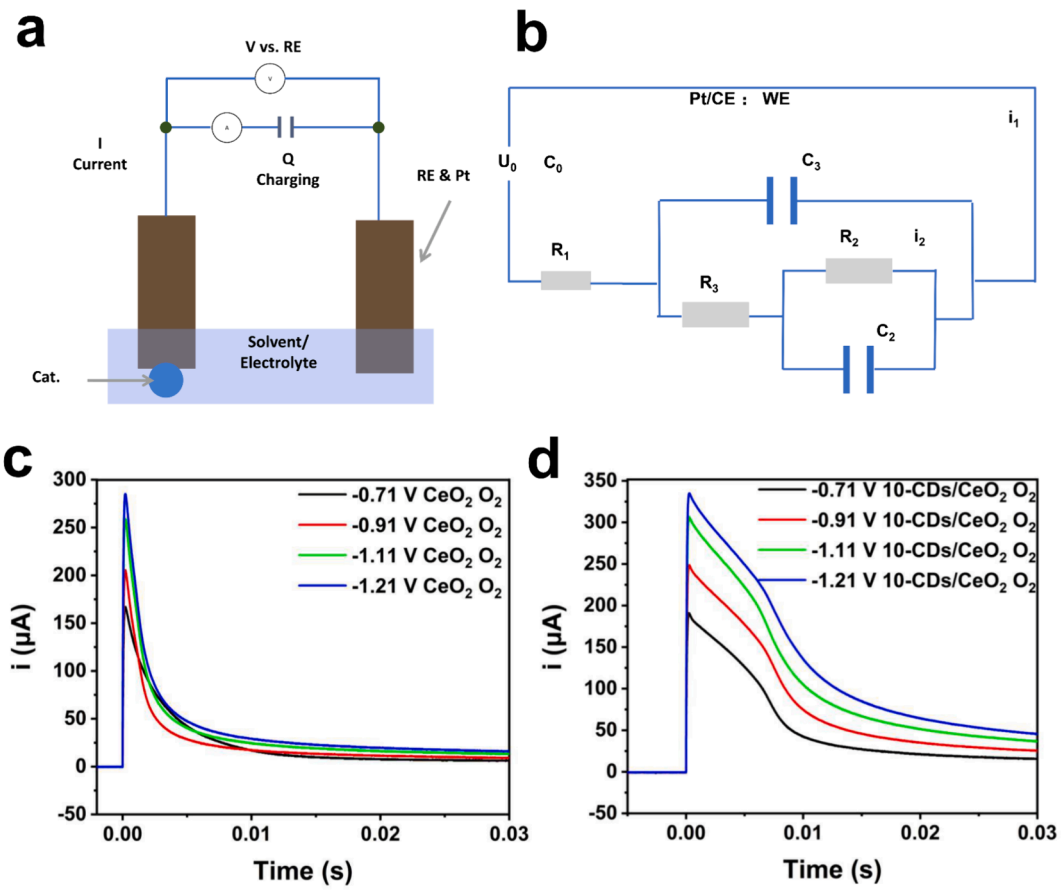


Fig. 4. (a) Schematic diagram and (b) Equivalent circuit of TPS test. TPS curves of (c) CeO_2 and (d) 10-CDs/CeO_2 under oxygen saturation conditions.

3.2. Electrochemical characterization

The selectivity of H_2O_2 was evaluated with a rotating ring disk electrode (RRDE) in a typical three-electrode system, and the electrochemical properties of $2e^-$ ORR were determined. All tests were performed in 0.1 M K_2SO_4 solution saturated with O_2. The linear scanning voltammetry (LSV) curves of five prepared samples are shown in Fig. 3a. The upper part of the LSV curve is annular current, and the lower part is disk current density. Notably, 10-CDs/CeO_2 had the highest ring current among the five samples, indicating that more H_2O_2 was generated at 10-CDs/CeO_2. Selectivity and electron transfer numbers for H_2O_2 were also calculated and plotted in Fig. 3b, c. 10-CDs/CeO_2 has the highest H_2O_2 selectivity at 0.18 V *vs* RHE, with 92.6 % H_2O_2 selectivity. The results show that the ORR catalyzed by 10-CDs/CeO_2 is almost dominated by $2e^-$ pathway. At the same time, the selectivity of 15-CDs/CeO_2 to H_2O_2 is slightly lower, about 89.6 %. The selectivity of CDs, CeO_2 and 5-CDs/CeO_2 for H_2O_2 was 62.9 %, 77.4 % and 90.6 %, respectively. Similarly, as shown in Fig. 3c, the electron transfer number of 10-CDs/CeO_2 is around 2.14, demonstrating again the dominance of the $2e^-$ ORR process. The electron transfer numbers of CDs, CeO_2, 5-CDs/CeO_2 and 15-CDs/CeO_2 are 2.75, 2.45, 2.19 and 2.20, respectively. Note that by comparing the LSV curves of CDs under N_2 and O_2 conditions, it can be seen that CDs bear a certain intrinsic activity and selectivity towards $2e^-$ ORR (Fig. S7). Upon coupling it with CeO_2, both of these two subunits displayed enhanced $2e^-$ ORR activity and selectivity, suggesting their co-catalytic feature. The electrochemically active surface areas (ECSA) of different samples were measured by double-layer capacitance (Figs. S8 and S9). With the increase of CDs content, the fitting slope increases, indicating that CDs can act as a co-catalyst and regulate the number of available active site of the catalyst. Importantly, the $2e^-$ ORR performance of 10-CDs/CeO_2 under neutral conditions was also compared with other reported literature, and its performance exceeded most previously documented catalysts (Table S1).

An accelerated durability test (ADT) was performed in O_2-saturated 0.1 M K_2SO_4 solution to evaluate the durability of 10-CDs/CeO_2. After 5 K ADT cycles, the weak current attenuation is shown in Fig. 3d, and the corresponding H_2O_2 selectivity (Fig. S10) and electron transfer number (Fig. 3e) are calculated. As was observed, 10-CDs/CeO_2 has excellent stability. The chronoamperometry method is also used to evaluate the long-term stability of 10-CDs/CeO_2, as shown in Fig. 3f. Even after 24 h of testing, the selectivity and activity degrade a little. The morphology of 10-CDs/CeO_2 after chrono-current test was observed by TEM, and the morphology was almost unchanged (Fig. S11). In addition, there is basically no shift in the XPS spectra of 10-CDs/CeO_2 after chrono-current testing, which proves the excellent stability of the catalyst (Fig. S12). These results suggest that 10-CDs/CeO_2 is a potential catalyst for H_2O_2 production in neutral media.

Although 10-CDs/CeO_2 had been shown to be a promising catalyst for H_2O_2 production, further testing of its capability to generate H_2O_2 on a large scale is still needed. Here we used H-Cell for testing to prove its good practicability. The 10-CDs/CeO_2 catalyst was loaded on carbon paper as a cathode and then assembled in an H-Cell filled with 0.1 M K_2SO_4 saturated with O_2 for H_2O_2 yield test. Chronoamperometry method (CA) was performed at a fixed potential RHE for 1800 s. The H_2O_2 yield was determined by potassium permanganate titration. The H_2O_2 yield of 10-CDs/CeO_2 was as high as 1000 mmol g_{cat}^{-1} h^{-1}. In addition, it achieved an excellent FE of about 97 %. In order to verify the accuracy of the determination of H_2O_2 concentration, eFOX solution standard colorimetry was used to determine the concentration of H_2O_2 during the catalysis process and the results were compared with potassium permanganate titration. Fig. S13 shows the ultraviolet absorption spectrum of the mixed solution. It can be seen that the absorbance at

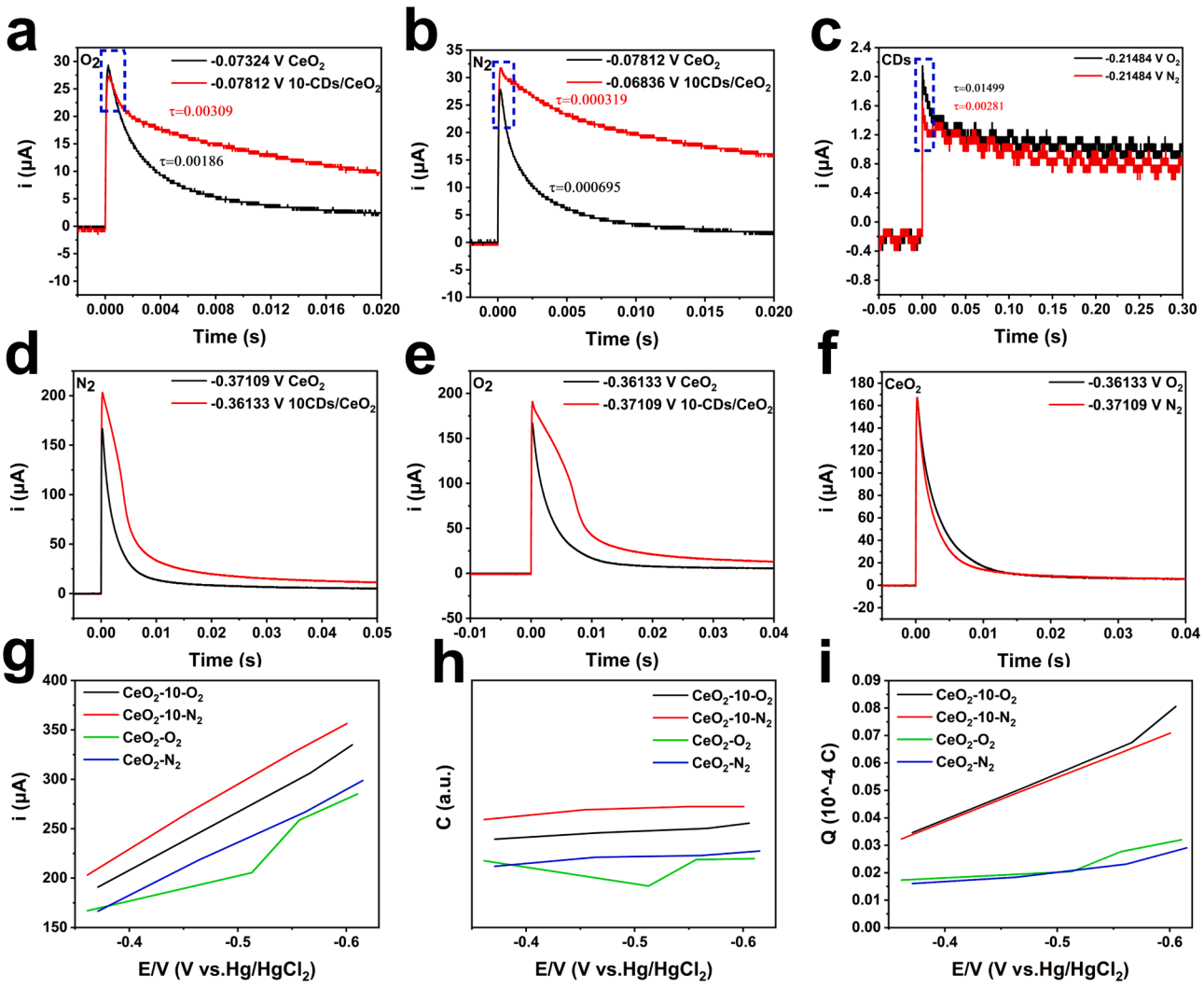


Fig. 5. (a–c) The current attenuation curves obtained by TPS test of different samples under different atmosphere and low potential. (d–e) The current decay curves obtained by TPS testing of different samples under different atmosphere Faraday potentials. (f) The current decay curves obtained by TPS test of CeO_2 under different atmosphere Faraday potential. (g) I_{MAX}-U curves obtained by TPS testing under different conditions. (h) C-U curves obtained by TPS testing under different conditions. (i) Q-U curves obtained by TPS testing under different conditions.

554 nm is 0.046569. H_2O_2 yield of catalysts is 920 mmol g_{cat}^{-1} h^{-1}. The above consistent results indicate that 10-CDs/CeO_2 holds practical application prospect in neutral electrosynthesis of H_2O_2.

To study the effects of CDs on electron transfer kinetics, an *in-situ* transient potential scanning (TPS) test was employed to analyze the kinetics of charge distribution during the dynamic reaction using a homemade device (Fig. 4a), which records sub-millisecond charging currents and their corresponding voltages. The schematic representation of the equivalent circuit for the TPS test is depicted in Fig. 4b. Capacitors C_0, C_2, and C_3 represent the external test capacitance, the catalyst surface state capacitance along with its pseudo-capacitance, and the interfacial double-layer capacitance, respectively. It should be noted that the solid space electric region capacitance of the catalyst C_1 is not considered here. Resistors R_1, R_2, and R_3 correspond to the electrode impedance, the faraday resistance associated with the catalytic reaction, and the interfacial resistance between the catalyst and the solution, respectively. The designated U_0 represents the initial charging potential applied to the test capacitor C_0. Once charged, the capacitor C_0 is connected to the catalytic system, with its positive terminal linked to the working electrode and the negative terminal to the counter electrode, enabling the measurement of the electrical current within the circuit. The TPS curves of the sample are shown in Fig. 4c, d. The voltage displayed on the i-t curve corresponds to the set voltage maintained throughout the TPS test. All profiles exhibit an initial decay from their maximum values, subsequently diminishing until equilibrium is reached.

To elucidate the influence of CDs on the $2e^-$ ORR process catalyzed by CeO_2, we integrated TPS findings with reaction mechanisms to discern their interactions. The TPS experiments were conducted under non-Faraday conditions for pristine CeO_2, CDs, and 10-CDs/CeO_2, at holding potentials of −0.11 V, −0.11 V, and −0.31 V *vs.* Hg/$HgCl_2$, respectively. The actual potentials, as marked in the current–time (I-T) curves, were determined from the potential-time (U-T) curves obtained during TPS, which are illustrated in Fig. S15–21. By fitting the initial segment of the decay curve on a microsecond timescale, we derived the decay constant (τ), which reflects the rate of charge dissipation within the system, as depicted in Fig. 5a-c. This approach ensures that the analysis of τ is isolated from the effects of prolonged reactions and solely represents the initial stages of charge decay. Under N_2-saturated environment, the τ for CeO_2, CDs, and 10-CDs/CeO_2 were recorded as 0.000695, 0.000319, and 0.01499 s, respectively. In contrast, under O_2-saturated conditions, these values shifted to 0.00186 s for CeO_2, 0.00281 s for CDs, and 0.00309 s for 10-CDs/CeO_2. Notably, the increased τ values under O_2 saturation indicate a slower charge decay

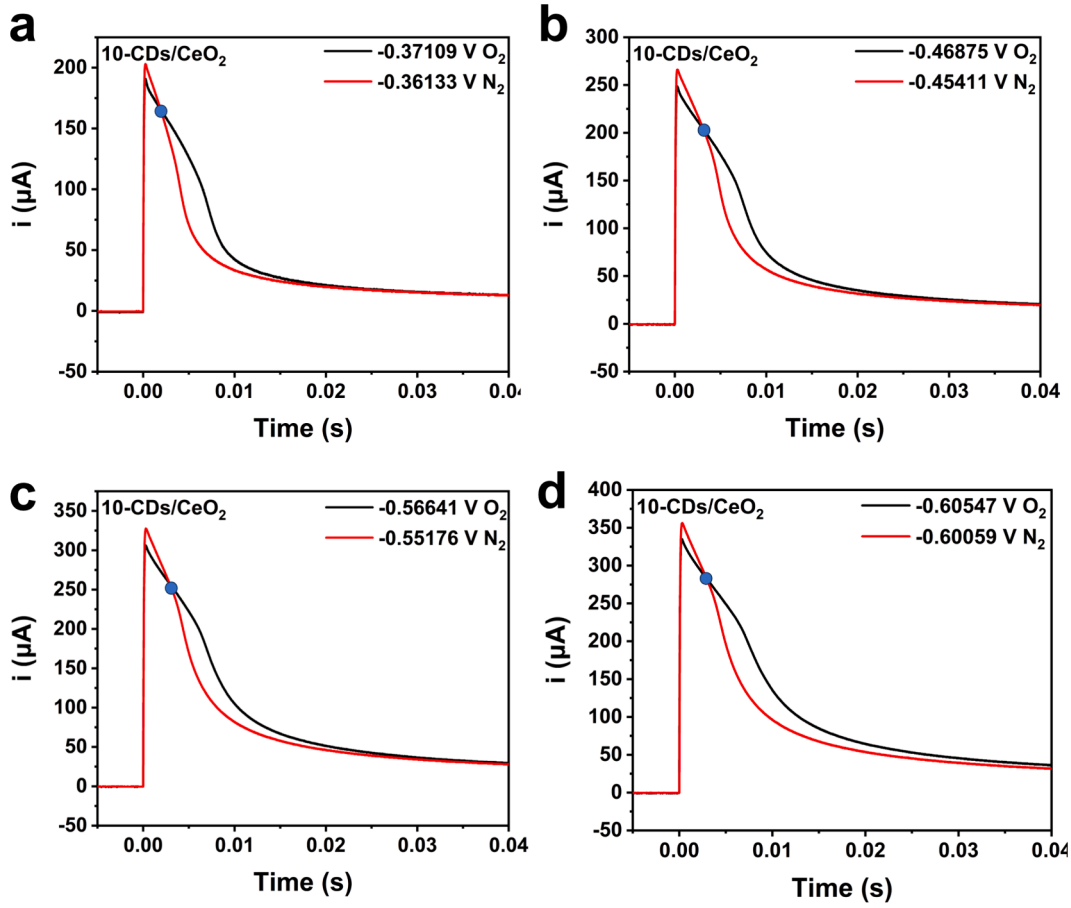


Fig. 6. TPS curves of CeO_2 for different atmospheres at (a) −0.37 V *vs.* $Hg/HgCl_2$, (b) −0.46 V *vs.* $Hg/HgCl_2$, (c) −0.56 V *vs.* $Hg/HgCl_2$ and (d) −0.60 V *vs.* $Hg/HgCl_2$ voltages.

rate due to the adsorption of oxygen, which may influence the formation of an electric double layer at the interface between the catalyst and the electrolyte. Conversely, under N_2 saturation, a rapid establishment of the interfacial double layer facilitates prompt electrical neutrality within the system. Furthermore, the significantly higher τ value for CDs compared to CeO_2 suggests that the charge transfer kinetics in the CDs/CeO_2 composite are predominantly governed by the CDs. This observation underscores the substantial role of CDs in modulating the electrochemical behavior of the composite material.

Furthermore, the TPS test at Faraday potential obtained the current–time curves of different samples under different atmospheres at different potentials (Fig. 5d, e and S22). Under the condition of N_2 saturation, it can be seen that the current of the composite CDs/CeO_2 is significantly stronger than that of CeO_2, and can maintain a high current state for a long time. However, the impedance of the composite CDs/CeO_2 is higher than that of CeO_2 (Fig. S23), which means that the charge storage capacity of the catalyst is the main factor determining the current intensity during the TPS test of the sample compared with the impedance. Therefore, we can judge that the composite CDs/CeO_2 has a stronger charge storage capacity (Fig. 5i). The negative correlation between large impedance and strong current shown by 10-CDs/CeO_2 should be attributed to the fact that its stronger charge storage capacity will redistribute the charge in the test system, and more charge will be transferred from the charging capacitor to the test system, thus exhibiting a larger current. In particular, the stronger charge storage capacity of 10-CDs/CeO_2 is favorable for delayed charge transfer, and its slower charge transfer kinetics is favorable for $2e^-$ ORR. Under the condition of O_2 saturation, we can see that the current of the composite CDs/CeO_2 is still significantly stronger than that of CeO_2, and the high current state is maintained for a longer time, which shows that the oxygen participating in the ORR reaction consumes the stored charge of the catalyst, so the charging capacitor needs to donate more charges to make the circuit current greater. According to the size of charge storage peak, the ORR reactivity of CDs/CeO_2 composites is obviously better than that of CeO_2 [39]. In addition, it can be observed that the maximum charging current (I_{MAX}) under N_2 condition is larger than that of under O_2 condition. This can be due to the increased impedance of the catalyst when exposed to an oxygen environment from the perspective of inherent electrical characteristics of a resistor–capacitor (RC) circuit (Fig. S23).

Comparison of the current–time profiles for CeO_2 under varying atmospheric conditions reveals that CeO_2 exhibits consistent behavior irrespective of the atmosphere, showing analogous characteristics in both N_2 and O_2 environments (Fig. 5f, S25). This suggests that the responsivity of the CDs/CeO_2 composite to oxygen is significantly influenced by CDs. To elucidate the impact of CDs on the $2e^-$ ORR, TPS measurements were conducted on CDs across different atmospheric conditions (Fig. S26). It was observed that the current response of CDs was amplified under an O_2-saturated atmosphere, attributed to an increase in sample capacitance due to oxygen adsorption onto the CDs (Fig. S27c). Conversely, over extended periods, the CDs exhibited a charge storage peak under an N_2 atmosphere, indicative of the formation of an interfacial double layer that enhances the charge storage capacity of the CDs. Under O_2 atmosphere, the CDs exhibited a rapid decay over time. This behavior is likely due to the influence of an electric double layer at the interface by oxygen adsorption, leading to a swift decline in current. Furthermore, even though the impedance of CDs was greater in the presence of O_2 compared to N_2 (as shown in Fig. S24), a higher I_{MAX} value was still noted in the O_2 environment than in the N_2 environment.

This discrepancy could be explained by a more substantial contribution from pseudo-capacitance in the case of CDs under oxygen conditions.

To thoroughly analyze the reaction dynamics of the composite CDs/CeO_2 over an extended period and the influence of CDs on CeO_2, we further compared the current–time curves of the composite under various atmospheric conditions and voltages (Fig. 6). Initially, it was observed that the current is higher under N_2 atmosphere due to the larger capacitance of the composite CDs/CeO_2 in the absence of oxygen (Fig. 5g, h). With time increasing, the current–time curves for the composite exhibit an intersection point. This intersection occurs because the oxygen participating in the ORR reaction depletes the charge of the composite CDs/CeO_2, consequently boosting the charging current. At this intersection, the rate at which charge is received, that is, the formation rate of the double electric layer at the catalyst interface aligns with the rate of charge consumption during the oxygen reaction. Once the charging potential stabilizes, the stable current reflects the rate at which the catalyst externally releases charge. By comparing the stable currents under different atmospheres and voltages across various samples, we note that the stable current is greater under O_2 atmosphere (Fig. S28), which is indicative of more charge being consumed by the ORR reaction. Furthermore, the stable current of CDs escalates more rapidly with voltage (Fig. S27d), suggesting that CDs facilitate a faster electron transfer within the composite CDs/CeO_2.

4. Conclusions

In our study, we developed the co-electrocatalysts based on CDs and CeO_2 for efficient $2e^-$ ORR in neutral media. The designed CDs/CeO_2 could exhibit the highest $2e^-$ selectivity of 92 %, substantially surpassing that of pristine CeO_2 (77 %), together with about 1.5 times enhancement of activity. Meanwhile, it also gained a high faraday efficiency of 97 % and a long durability at 20 mA cm^{-2} for 24 h. To better understand how the movement of electrons affects the process of the catalytic process of CDs/CeO_2, we used TPS technology as one powerful kinetic analysis tool to show that CDs could effectively control how charges were distributed in the reaction system, including the effects of oxygen binding to the catalyst, the ability of one catalyst to store electrons, and how quickly electrons move. Appropriate incorporation of CDs could greatly contribute to the reaction kinetics and thermodynamics, thus the enhancement of the selectivity and activity of CeO_2. This work is expected to offer fresh ideas for creating more efficient catalysts in the future.

CRediT authorship contribution statement

Weijie Yuan: Investigation. **Jiacheng Li:** Data curation. **Huiyu Yang:** Methodology. **Ziliang Chen:** Writing – review & editing, Writing – original draft, Supervision, Resources, Formal analysis. **Zhiwei Liu:** Investigation. **Hui Huang:** Writing – review & editing, Writing – original draft, Supervision, Resources, Conceptualization. **Yang Liu:** Writing – original draft, Resources. **Zhenhui Kang:** Writing – review & editing, Supervision, Project administration.

Declaration of competing interest

The authors declare that they have no known competing financial interests or personal relationships that could have appeared to influence the work reported in this paper.

Acknowledgements

This work is supported by Natural Science Foundation of Jiangsu Province (BK20220028), National Key R&D Program of China (2020YFA0406104, 2020YFA0406101), National Natural Science Foundation of China (52271223, 52202107, 52201269, 52272043), Natural Science Foundation of Jiangsu Province (BK20210735, 21KJB430043), The Science and Technology Development Fund, Macau SAR (0009/2022/ITP), Shenzhen Science and Technology Plan Project (Collaborative Innovation Special Project, SGDX20220530111203019), Collaborative Innovation Center of Suzhou Nano Science & Technology, the 111 Project, and Suzhou Key Laboratory of Functional Nano & Soft Materials.

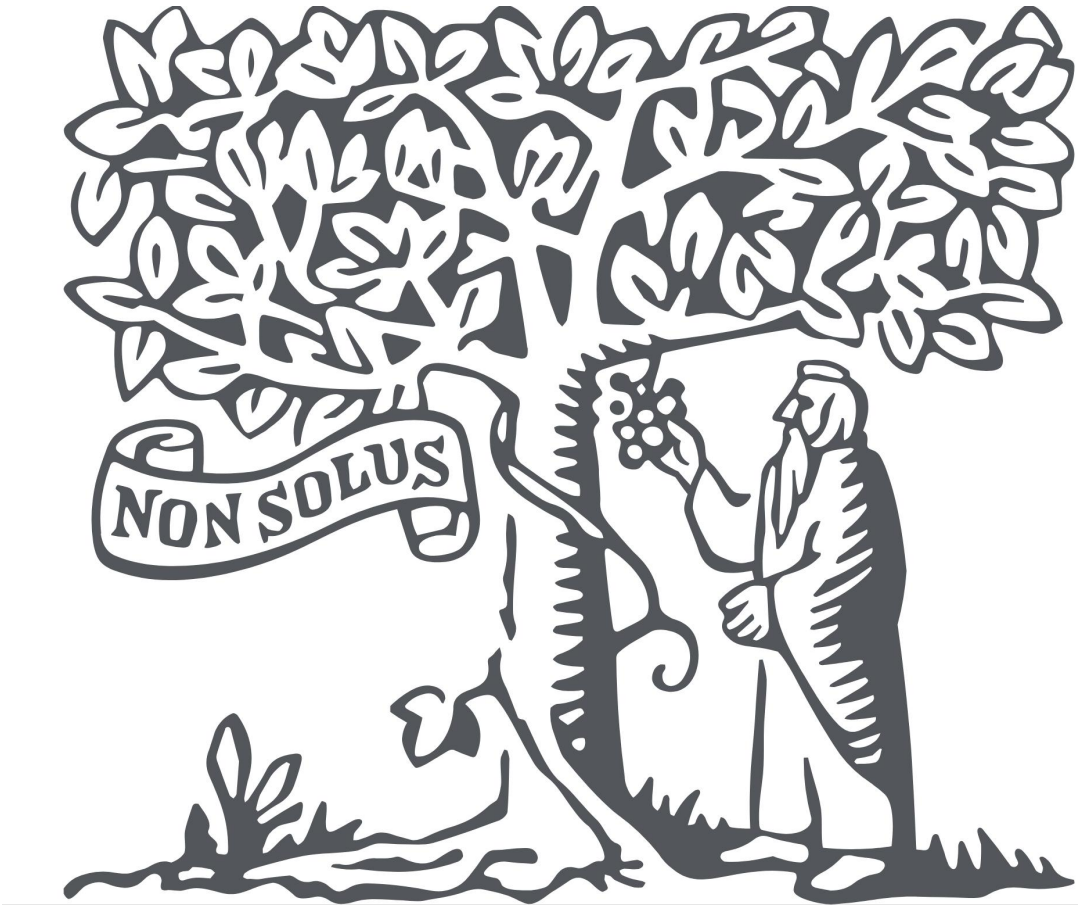
Appendix A. Supplementary data

Supplementary data (additional figures) to this article can be found online at https://doi.org/10.1016/j.jelechem.2024.118604.

References

[1] M. Song, W. Liu, J.J. Zhang, C. Zhang, X. Huang, D.L. Wang, Single-atom catalysts for H_2O_2 electrosynthesis via two-electron oxygen reduction reaction, Adv. Funct. Mater. 33 (2023) 2212087.
[2] C.H. Jiang, Y.F. Fei, W.W. Xu, Z.K. Bao, Y.Z. Shao, S.J. Zhang, Z.T. Hu, J.G. Wang, Synergistic effects of Bi_2O_3 and Ta_2O_5 for efficient electrochemical production of H_2O_2, Appl. Catal. B: Environ. 334 (2023) 122867.
[3] Q. Wang, L.P. Ren, J. Zhang, X. Chen, C.Y. Chen, F. Zhang, S. Wang, J. Chen, J. J. Wei, Recent progress on the catalysts and device designs for (Photo) electrochemical on-site H_2O_2 production, Adv. Energy Mater. 13 (2023) 2301543.
[4] H. Luo, T.S. Shan, J.W. Zhou, L.L. Huang, L.H. Chen, R. Sa, Y. Yamauchi, J.M. You, Y. Asakura, Z.H. Yuan, H. Xiao, Controlled synthesis of hollow carbon ring incorporated g-C_3N_4 tubes for boosting photocatalytic H_2O_2 production, Appl. Catal. B: Environ. 337 (2023) 122933.
[5] W.M. Zhou, Z.Q. Wang, H.Q. Huang, Y.T. Wu, A.A. Alothman, M. Ouladsmane, Y. Yamauchi, X.T. Xu, M. An, L.W. Wang, Z.H. Yuan, Significant enhancement in hydrogen evolution rate of 2D bismuth oxychloride lamellar membrane photocatalyst with cellulose nanofibers, Chem. Eng. J. 456 (2023) 140933.
[6] A.B. Abdeta, Q.H. Wu, D.H. Kuo, P. Li, H.Y. Zhang, J.B. Zhang, Z.H. Yuan, J.G. Lin, X.Y. Chen, Activated carbon-supported AgMoOS bimetallic oxysulfide as a catalyst for the photocatalytic hydrogen evolution and pollutants reduction, J. Alloy. Compd. 913 (2022) 165287.
[7] X.X. Yang, Y.C. Zeng, W. Alnoush, Y. Hou, D. Higgins, G. Wu, Tuning two-electron oxygen-reduction pathways for H_2O_2 electrosynthesis via engineering atomically dispersed single metal site catalysts, Adv. Mater. 34 (2022) 2107954.
[8] S.C. Sun, W.M. Zhou, L.Y. Wang, M.X. Zhang, I. Lawan, L.W. Wang, F. Zhang, M. Lin, Z.H. Yuan, Oxygen-vacancy engineering approach to bismuth basic nitrate/g-C_3N_4 heterostructure for efficiently photocatalytic hydrogen evolution, Int. J. Hydrogen Energy 46 (2021) 25832–25842.
[9] S.W. Sharshir, M.A. Farahat, A. Joseph, A.W. Kandeal, M.A. Rozza, F. Abou-Taleb, A.E. Kabeel, Z.H. Yuan, Comprehensive thermo-enviroeconomic performance analysis of a preheating-assisted trapezoidal solar still provided with various additives, Desalination 548 (2023) 116280.
[10] R.T. Gao, L.J. Liu, Y.B. Li, Y. Yang, J.L. He, X.H. Liu, X.Y. Zhang, L. Wang, L.M. Wu, Ru- P pair sites boost charge transport in hematite photoanodes for exceeding 1% efficient solar water splitting, Proc. Natl. Acad. Sci. USA 120 (2023) e2300493120.
[11] Z.L. Chen, J. Wu, Z.R. Chen, H.Y. Yang, K. Zou, X.Y. Zhao, R.H. Liang, X.L. Dong, P. W. Menezes, Z.H. Kang, Entropy enhanced perovskite oxide ceramic for efficient electrochemical reduction of oxygen to hydrogen peroxide, Angew. Chem. Int. Edit. 61 (2022) e202200086.
[12] H.Y. Yang, J. Wu, Z.R. Chen, K. Zou, R.H. Liang, Z.H. Kang, P.W. Menezes, Z. L. Chen, A dynamic piezoelectric effect to promote electrosynthesis of hydrogen peroxide, Energy Environ. Sci. 16 (2023) 210–221.
[13] L.Y. Jing, Q. Tian, W.Y. Wang, X. Li, Q. Hu, H.P. Yang, C.X. He, Unveiling favorable microenvironment on porous doped carbon nanosheets for superior H_2O_2 electrosynthesis in neutral media, Adv. Energy Mater. (2023) 2304418.
[14] Y.J. Zhou, L. Xu, J. Wu, W.X. Zhu, T.W. He, H. Yang, H. Huang, T. Cheng, Y. Liu, Z. H. Kang, The operation active sites of O_2 reduction to H_2O_2 over ZnO, Energy Environ. Sci. 16 (2023) 3526–3533.
[15] R.D. Ross, H.Y. Sheng, Y.J. Ding, A.N. Janes, D.W. Feng, J.R. Schmidt, C.U. Segre, S. Jin, Operando elucidation of electrocatalytic and redox mechanisms on a 2D metal organic framework catalyst for efficient electrosynthesis of hydrogen peroxide in neutral media, J. Am. Chem. Soc. 144 (2022) 15845–15854.
[16] N. Wang, S.B. Ma, R.Y. Zhang, L.F. Wang, Y.A. Wang, L.H. Yang, J.H. Li, F. Guan, J. Z. Duan, B.R. Hou, Regulating N species in N-Doped carbon electro-catalysts for high-efficiency synthesis of hydrogen peroxide in simulated seawater, Adv. Sci. 10 (2023) 2302446.
[17] Y.J. Zhao, H. Wang, J. Li, Y. Fang, Y.S. Kang, T.Y. Zhao, C.Y. Zhao, Regulating the spin-state of rare-earth Ce single atom catalyst for boosted oxygen reduction in neutral medium, Adv. Funct. Mater. 33 (2023) 2305268.
[18] X. Luo, M. Yan, W.Y. Song, Q. Fang, X.Q. Wei, L. Jiao, W.Q. Xu, Y.K. Kang, H. J. Wang, N.N. Wu, W.L. Gu, L.R. Zheng, L.Y. Hu, C.Z. Zhu, Neutral Zn-air battery assembled with single-atom iridium catalysts for sensitive self-powered sensing system, Adv. Funct. Mater. 31 (2021) 2101193.
[19] R. Xu, X.K. Wang, M.Z. Sun, C.H. Zhang, C. Li, Z.W. Cao, M. Gu, B.L. Huang, M. H. Huang, Promoting oxygen reduction kinetics of single Fe sites for robust neutral Zn-air batteries via engineering synergistic Fe nanocluster as proton-feeding center, Chem. Eng. J. 475 (2021) 146065.

[20] X.C. Chai, R.T. Gao, L. Wang, Electron transport kinetics via ZnO with ultralow Fe dopant for stable oxygen reduction to H_2O_2, Chem. Eng. J. 484 (2024) 149527.
[21] H. Yang, N. An, Z. Kang, P.W. Menezes, Z. Chen, Understanding advanced transition metal-based two electron oxygen reduction electrocatalysts from the perspective of phase engineering, Adv. Mater. (2024) 2400140.
[22] Y. Jiang, H. Fu, Z. Liang, Q. Zhang, Y.P. Du, Rare earth oxide based electrocatalysts: synthesis, properties and applications, Chem. Soc. Rev. 53 (2024) 714–763.
[23] C.Y. Li, P. Wang, M. He, X.L. Yuan, Z. Fang, Z.X. Li, Rare earth-based nanomaterials in electrocatalysis, Coord. Chem. Rev. 489 (2023) 215204.
[24] I. Hota, A.K. Debnath, K.P. Muthe, K.S.K. Varadwaj, P. Parhi, Electrocatalytic production of hydrogen-peroxide from molecular oxygen by rare earth (Pr, Nd, Sm or Gd) Oxide nanorods, Electroanal. 32 (2020) 2521–2527.
[25] M. Cheng, Z.G. Li, T.X. Xu, Y.X. Mao, Y. Zhang, G.X. Zhang, Z.F. Yan, Efficient overall $2e^-$ oxygen electrolysis to H_2O_2 on CeO_2 nanocubes, Electrochim. Acta. 430 (2022) 141091.
[26] H.X. Liu, X. Zhong, Q. Pan, Y. Zhang, W.T. Deng, G.Q. Zou, H.S. Hou, X.B. Ji, A review of carbon dots in synthesis strategy, Coord. Chem. Rev. 498 (2024) 215468.
[27] Z.L. Chen, Y. Liu, Z.H. Kang, Diversity and tailorability of photoelectrochemical properties of carbon dots, Acc. Chem. Res. 55 (2022) 3110–3124.
[28] H. Yuan, H.R. Sun, Y.X. Shi, J.X. Wang, A. Bian, Y.Y. Hu, F. Guo, W.L. Shi, X. Du, Z. H. Kang, Cooperation of carbon doping and carbon loading boosts photocatalytic activity by the optimum photo-induced electron trapping and interfacial charge transfer, Chem. Eng. J. 472 (2023) 144654.
[29] H.Q. Song, Y.H. Li, L. Shang, Z.Y. Tang, T.R. Zhang, S.Y. Lu, Designed controllable nitrogen-doped carbon-dots-loaded MoP nanoparticles for boosting hydrogen evolution reaction in alkaline medium, Nano Energy 72 (2020) 104730.
[30] J. Wu, Y.D. Han, Y.C. Bai, X.T. Wang, Y.J. Zhou, W.X. Zhu, T.W. He, Y.M. Wang, H. Huang, Y. Liu, Z.H. Kang, The electron transport regulation in carbon dots/In_2O_3 electrocatalyst enable 100 % selectivity for oxygen reduction to hydrogen peroxide, Adv. Funct. Mater. 32 (2022) 2203647.
[31] Z.H. Sun, Y.K. Wang, L.B. Zhang, H. Wu, Y.C. Jin, Y.H. Li, Y.C. Shi, T.X. Zhu, H. Mao, J.M. Liu, C.H. Xiao, S.J. Ding, Simultaneously realizing rapid electron transfer and mass transport in jellyfish-like Mott-Schottky nanoreactors for oxygen reduction reaction, Adv. Funct. Mater. 30 (2020) 1910482.
[32] Y.H. Wu, Q.X. Yuan, Y.Y. Zhao, X. Xu, J. Xu, Y. Wang, K. Sun, A. Wang, H. Sun, B. Li, R.T. Xu, Z.M. Wang, J.C. Jiang, M.M. Fan, Boron-sulfur pairs for highly active $2e^-$ oxygen reduction reaction to electrochemically synthesize hydrogen peroxide, ACS Sustain. Chem. Eng. 11 (2023) 13363–13373.
[33] M.V. Sreejith, J.R. Thomas, C. T. Characterisation of atmospheric particulate matter over a site in southern Kerala, India - using ATR-FTIR and confocal Micro-Raman spectroscopy, Mater. Today: Proc. 33 (2020) 1410-1414.
[34] P. Kumar Mahato, S. Choudhuri, C. Kumar, S. Roy, P. Patra, Evaluation of crystal size present in graphene oxide quantum dots using optical and Raman spectroscopy, Mater. Today: Proc. 80 (2023) 668-673.
[35] G. Wang, Q. Mu, T. Chen, Y. Wang, Synthesis, Characterization and photoluminescence of CeO_2 nanoparticles by a facile method at room temperature, J. Alloys Compds. 493 (2010) 202–207.
[36] X. Chen, X. Wang, D. Fang, A review on C1s XPS-spectra for some kinds of carbon materials, Fuller. Nanotube. Car. N. 28 (2020) 1048–1058.
[37] H. Aono, E. Traversa, M. Sakamoto, Y. Sadaoka, Crystallographic characterization and NO_2 gas sensing property of $LnFeO_3$ prepared by thermal decomposition of Ln-Fe hexacyano-complexes, $Ln[Fe(CN)_6]\bullet nH_2O$, Ln = La, Nd, Sm, Gd, and Dy, Sensor, Actuat. B-Chem. 94 (2003) 132–139.
[38] A. Pfau, K.D. Schierbaum, The electronic-structure of stoichiometric and reduced CeO_2 surfaces - an XPS, UPS and HREELS Study, Surf. Sci. 321 (1994) 71–80.
[39] K. Qin, H. Yu, W. Zhu, Y. Zhou, Z. Guo, Q. Shao, Y. Wu, X. Wang, Y. Li, Y. Ji, F. Liao, Y. Liu, Z. Kang, M. Shao, 1D Monoclinic IrxRu1-xO_2 solid solution with Ru-enhanced electrocatalytic activity for acidic oxygen evolution reaction, Adv. Funct. Mater. (2024) 2402226.
[40] Z.N. Li, T.Y. Zhang, J. Shen, Y.R. Ma, K. Yu, J.C. Li, H. Huang, Y. Liu, Z.H. Kang, Highly efficient photo-driven generation and elimination of reactive oxygen species in biological environment by gold nanoclusters, J. Environ. Chem. Eng. 11 (2023) 111546.


NON SOLUS

创新创业学分认定诚信声明

本人郑重声明：所提交的用以申请创新创业学分认定的内容(包括但不限于学科竞赛获奖、学术论文、科研项目成果、专利创造成果、文学艺术类成果以及创业实践类成果等)均为本人在校期间原创取得，不存在任何侵权、造假等违规行为。

本人完全意识到本声明的法律后果由本人承担。本人所提交的内容如涉嫌违规违法，本人愿意承担相应后果。

申请人签名：杨慧雨

指导（证明）老师签名：

2024年6月 5 日

专家鉴定意见

本人作为纳米材料与技术领域的专业研究人员，经审核确认，Enhanced electron transfer kinetics via constructing co-catalytic system of cerium oxide and carbon dots enabling efficient electrosynthesis of hydrogen peroxide in neutral media 围绕电催化性能研究展开，与纳米材料与技术专业核心方向高度契合。

本人作为指导老师，对成果的原创性、真实性及学术规范性予以确认。

推荐人签名：

2025 年 6 月 9 号